MOX-Report No. 34/2025

Coupling models of resistive valves to muscle mechanics in cardiac fluid-structure interaction simulations

Bucelli, M.; Dede', L.

Coupling models of resistive valves to muscle mechanics in cardiac fluid-structure interaction simulations

Michele Bucelli[a,*], Luca Dede'[a]

[a]*MOX Laboratory of Modeling and Scientific Computing, Dipartimento di Matematica, Politecnico di Milano, Piazza Leonardo da Vinci 32, 20133, Milano, Italy*

Abstract

To accurately simulate all phases of the cardiac cycle, computational models of hemodynamics in heart chambers need to include a sufficiently faithful model of cardiac valves. This can be achieved efficiently through resistive methods, and the resistive immersed implicit surface (RIIS) model in particular [Fedele et al., BMMB, 2017]. However, the conventional RIIS model is not suited to fluid-structure interaction (FSI) simulations, since it neglects the reaction forces by which valves are attached to the cardiac walls, leading to models that are not consistent with Newton's laws. In this paper, we propose an improvement to RIIS to overcome this limitation, by adding distributed forces acting on the structure to model the attachment of valves to the cardiac walls. The modification has a minimal computational overhead thanks to an explicit numerical discretization scheme. Numerical experiments in both idealized and realistic settings demonstrate the effectiveness of the proposed modification in ensuring the physical consistency of the model, thus allowing to apply RIIS and other resistive valve models in the context of FSI simulations.

Keywords: fluid-structure interaction, cardiac modeling, valve modeling, resistive immersed implicit surface

1. Introduction

The motion of cardiac valves, both native and prosthetic, is regulated by the complex and dynamic interplay of blood flow with the mechanics of valve leaflets. A physically detailed computational model of valves must be able to deal with large deformations, the effect of chordae tendineae, and the contact among valve leaflets themselves [14, 21, 27, 35, 37–39, 50, 56, 58, 64]. These aspects, although crucial when focusing on valve dynamics or valvular dysfunctions, pose a significant challenge in terms of model calibration, complexity, and computational cost.

As an alternative, it is possible to use valve models that are simplified, geometrically (e.g. using a planar representation of the valve), physically (by neglecting fluid-structure interaction (FSI)), or both [15, 60, 61]. This is especially convenient for models that do not focus on the valves themselves, but only need to account for the macroscopic effect of the valves on the flow within heart chambers, such as the way their opening and closing determines heartbeat phases [13], or the large-scale jets and vortices caused by valve leaflets [49, 65]. Simplified models may be sufficiently accurate to capture these features, yet at a manageable complexity and cost.

Many such models are based on a resistive approach, by which the equations for fluid flow are modified to penalize the mismatch between the fluid velocity and valve velocity in the proximity of the valve. This corresponds to modeling the valve as a porous medium with very low permeability [20]. For example, valves are modeled in [36] through Navier-Stokes-Brinkman (NSB) equations, assuming a planar geometry. The Resistive Immersed Surface (RIS) method [5, 47, 57] represents valves as resistive surfaces, which are assumed to be conforming to the mesh used to discretize fluid equations. In both NSB and RIS, the opening and

---

[*] Corresponding author. E-mail: michele.bucelli@polimi.it

closing of the valve may be modeled by varying the associated penalization coefficient (i.e. its permeability) over time.

In this work, we consider the Resistive Immersed Implicit Surface (RIIS) method [24], which relaxes the mesh-conformity constraint of RIS by implicitly representing valves through signed distance functions. This allows to represent the valve leaflets as they open and close, regardless of the underlying mesh. The RIIS method was extensively applied to cardiovascular hemodynamics simulations [13, 16, 19, 23, 29, 41, 62, 63, 65], showcasing its effectiveness in supporting detailed and patient-specific [8, 9, 18, 30, 46] computational models.

However, in the specific context of models that include FSI between blood and the cardiac walls, the RIIS method (and resistive methods in general) may lead to issues in the balance of forces. Indeed, resistive surfaces exert a force on the fluid, to enforce the no-slip condition in proximity of the valve. In real hearts, this force is sustained by the attachment of valves to the walls, through either the chordae tendineae or the valve annuli. By simply applying the RIIS method in its original form, this is neglected, which leads to a force imbalance and possibly to an unphysical behavior of the FSI system as a whole. This can be compensated through an ad-hoc calibration of other parameters, most notably the boundary conditions on the mechanics model, as done in [13]. However, this approach lacks in physical soundness: the application of standard RIIS in the FSI context leads to models that do not satisfy Newton's laws.

In this paper, we propose an improvement to the RIIS method for FSI that accounts for the forces keeping the valves attached to the cardiac walls. After deriving an expression for these forces, we demonstrate through numerical experiments how neglecting them may lead to unphysical displacements, and how the proposed modification eliminates this issue. We remark that, with minor modifications, the proposed method can be extended to other resistive valve models, which may face the same issue when combined with FSI simulations.

The remainder of this paper is structured as follows. In Section 2, we present the mathematical models used for cardiac FSI, introduce the modifications for coupling resistive valves to solid mechanics, and discuss numerical discretization. Section 3 illustrates the properties of the proposed modification through numerical experiments. Finally, Section 4 draws some conclusive remarks.

2. Models and methods

This section describes the modeling and discretization framework employed for cardiac FSI simulations, and presents the approach proposed in this work to couple resistive valves and muscular mechanics.

2.1. Cardiac fluid-structure interaction modeling

Let $t \in (0, T)$ denote the independent time variable, with $T > 0$. Let $\Omega \subset \mathbb{R}^3$ be an open set, moving over time, representing the volume occupied by a beating heart. We partition Ω into two subsets, Ω_f and Ω_s, representing the volume occupied by the blood inside the heart cavities and by the cardiac walls, respectively. Notice that the set Ω_s does not include the cardiac valve leaflets, which are instead accounted for through a resistive approach, and are thus immersed in Ω_f, as detailed below. Let $\Sigma = \partial\Omega_\mathrm{f} \cap \partial\Omega_\mathrm{s}$ denote the fluid-solid interface.

To track the deformation of the domain in time, we introduce the fixed reference domain $\widehat{\Omega} \subset \mathbb{R}^3$, as well as its subsets $\widehat{\Omega}_\mathrm{f}$ and $\widehat{\Omega}_\mathrm{s}$. The current domains Ω_f and Ω_s are related to the reference domains through the continuous maps [13]

$$\boldsymbol{\psi}_\mathrm{f} : \widehat{\Omega}_\mathrm{f} \times (0, T) \to \Omega_\mathrm{f} \;,$$
$$\boldsymbol{\psi}_\mathrm{s} : \widehat{\Omega}_\mathrm{s} \times (0, T) \to \Omega_\mathrm{s} \;.$$

Henceforth, we shall use a hat to denote functions and sets in the reference configuration, without a hat their counterparts mapped onto the current configuration, and vice versa.

We consider an FSI model of the displacement of the cardiac walls and the blood flow [12, 13], based on the arbitrary Lagrangian-Eulerian (ALE) formulation of incompressible Navier-Stokes equations [22, 33] and on a hyperelastic model for muscular mechanics, including active stress [45]. The model features the following unknowns:

$$\widehat{\mathbf{d}}_\mathrm{ALE} : \widehat{\Omega}_\mathrm{f} \times (0, T) \to \mathbb{R}^3 \qquad \text{fluid domain displacement,}$$

$$\begin{aligned}
&\mathbf{u} : \Omega_\mathrm{f} \times (0,T) \to \mathbb{R}^3 && \text{blood velocity,} \\
&p : \Omega_\mathrm{f} \times (0,T) \to \mathbb{R} && \text{blood pressure,} \\
&\widehat{\mathbf{d}} : \widehat{\Omega}_\mathrm{s} \times (0,T) \to \mathbb{R}^3 && \text{solid displacement.}
\end{aligned}$$

The fluid domain displacement is computed by extending the solid displacement from the fluid-solid interface $\widehat{\Sigma}$ to the whole $\widehat{\Omega}_\mathrm{f}$, by solving the following problem [51]:

$$\begin{cases}
\mathcal{L}_\mathrm{ALE}(\widehat{\mathbf{d}}_\mathrm{ALE}) = \mathbf{0} & \text{in } \widehat{\Omega}_\mathrm{f} \times (0,T)\;, \\
\widehat{\mathbf{d}}_\mathrm{ALE} = \widehat{\mathbf{d}} & \text{on } \widehat{\Sigma} \times (0,T)\;, \\
\widehat{\mathbf{d}}_\mathrm{ALE} = \mathbf{0} & \text{on } (\partial\widehat{\Omega}_\mathrm{f} \backslash \widehat{\Sigma}) \times (0,T)\;,
\end{cases}$$

where $\mathcal{L}_\mathrm{ALE}$ is a suitable differential operator. At any time $t \in (0,T)$, the fluid domain in its current configuration is obtained by setting

$$\begin{aligned}
\boldsymbol{\psi}_\mathrm{f}(\widehat{\mathbf{x}}, t) &= \widehat{\mathbf{x}} + \widehat{\mathbf{d}}_\mathrm{ALE}(\widehat{\mathbf{x}}, t)\;, \\
\Omega_\mathrm{f} &= \left\{ \mathbf{x} \in \mathbb{R}^3 : \mathbf{x} = \boldsymbol{\psi}_\mathrm{f}(\widehat{\mathbf{x}}, t),\ \widehat{\mathbf{x}} \in \widehat{\Omega}_\mathrm{f} \right\}\;.
\end{aligned}$$

The evolution of blood velocity and pressure is prescribed by the incompressible Navier-Stokes equations, in ALE formulation:

$$\begin{cases}
\rho_\mathrm{f} \dfrac{\partial \mathbf{u}}{\partial t} + \rho_\mathrm{f}\left((\mathbf{u} - \mathbf{u}_\mathrm{ALE}) \cdot \boldsymbol{\nabla}\right)\mathbf{u} - \boldsymbol{\nabla} \cdot \sigma_\mathrm{f}(\mathbf{u}, p) + \mathbf{R}(\mathbf{u}, \mathbf{u}_\mathrm{ALE}) = \mathbf{0} & \text{in } \Omega_\mathrm{f} \times (0,T)\;, \\
\boldsymbol{\nabla} \cdot \mathbf{u} = 0 & \text{in } \Omega_\mathrm{f} \times (0,T)\;.
\end{cases} \tag{1}$$

In the above, ρ_f is the blood density, $\sigma_\mathrm{f}(\mathbf{u}, p) = \mu(\boldsymbol{\nabla}\mathbf{u} + \boldsymbol{\nabla}^T\mathbf{u}) - pI$ is the Cauchy stress tensor, with μ the blood viscosity, and $\mathbf{u}_\mathrm{ALE} : \Omega_\mathrm{f} \times (0,T) \to \mathbb{R}^3$ is the known domain velocity, defined as

$$\mathbf{u}_\mathrm{ALE}(\mathbf{x}, t) = \frac{\partial \widehat{\mathbf{d}}_\mathrm{ALE}}{\partial t}\;.$$

The term $\mathbf{R}(\mathbf{u}, \mathbf{u}_\mathrm{ALE})$ accounts for the presence of cardiac valves through the RIIS method [24, 30, 63].

Let N_v be the number of valves present in the model. Each valve is represented in reference configuration by a surface $\widehat{\Gamma}_k$ (for $k = 1, \dots, N_\mathrm{v}$) immersed in the fluid domain (i.e. such that $\Gamma_k \cap \widehat{\Omega}_\mathrm{f} \neq \varnothing$). Each surface $\widehat{\Gamma}_k$ moves following the fluid domain displacement $\widehat{\mathbf{d}}_\mathrm{ALE}$, and it opens and closes according to a prescribed displacement field $\mathbf{d}_k : \widehat{\Gamma}_k \times (0,T) \to \mathbb{R}^3$. Therefore, at any time $t \in (0,T)$, the current configuration of the valve is given by

$$\Gamma_k = \left\{ \mathbf{x} \in \mathbb{R}^3 : \mathbf{x} = \widehat{\mathbf{x}} + \widehat{\mathbf{d}}_\mathrm{ALE}(\widehat{\mathbf{x}}, t) + \mathbf{d}_k(\widehat{\mathbf{x}}, t), \widehat{\mathbf{x}} \in \widehat{\Gamma}_k \right\}\;.$$

The resistive term $\mathbf{R}(\mathbf{u}, \mathbf{u}_\mathrm{ALE}) \in \mathbb{R}^3$ in (1) has the purpose of weakly enforcing a no-slip condition in the vicinity of the valve surface. Following [13, 63], we neglect the valve velocity due to changes in valve configuration, which corresponds to assuming $\frac{\partial \mathbf{d}_k}{\partial t} \approx \mathbf{0}$. Therefore, the valve velocity equals $\mathbf{u}_\mathrm{ALE}$, and the resistive term must penalize the mismatch between $\mathbf{u}$ and $\mathbf{u}_\mathrm{ALE}$. It is defined as:

$$\mathbf{R}(\mathbf{u}, \mathbf{u}_\mathrm{ALE}) = \sum_{k=1}^{N_\mathrm{v}} \mathbf{R}_k(\mathbf{u}, \mathbf{u}_\mathrm{ALE})\;, \tag{2}$$

$$\mathbf{R}_k(\mathbf{u}, \mathbf{u}_\mathrm{ALE}) = \frac{R_k}{\varepsilon_k} \delta_k(\varphi_k(\mathbf{x}))(\mathbf{u} - \mathbf{u}_\mathrm{ALE})\;. \tag{3}$$

In the above, R_k is the valve resistance, $\varepsilon_k > 0$ is the half-thickness of the k-th valve, φ_k is the distance function from the current configuration of the surface Γ_k, and δ_k is a smoothed Dirac delta function, defined as

$$\delta_k(y) = \begin{cases}
\dfrac{1}{2\varepsilon_k}\left(1 + \cos\left(\dfrac{\pi y}{\varepsilon_k}\right)\right) & \text{if } |y| \leq \varepsilon\;, \\
0 & \text{otherwise.}
\end{cases}$$

The evolution of muscular displacement is prescribed by the following elastodynamics equation in Lagrangian reference:

$$\rho_{\mathrm{s}} \frac{\partial^2 \widehat{\mathbf{d}}}{\partial t^2} - \boldsymbol{\nabla} \cdot \mathbf{P}_{\mathrm{s}}(\widehat{\mathbf{d}}, t) = \mathbf{0} \qquad \text{in } \widehat{\Omega}_{\mathrm{s}} \times (0, T) \;, \tag{4}$$

wherein $\mathbf{P}_{\mathrm{s}}$ is the first Piola-Kirchhoff stress tensor. The stress tensor is decomposed as the sum of an active and a passive contribution, i.e.

$$\mathbf{P}_{\mathrm{s}}(\widehat{\mathbf{d}}, t) = \mathbf{P}_{\mathrm{s}}^{\mathrm{act}}(\widehat{\mathbf{d}}, t) + \mathbf{P}_{\mathrm{s}}^{\mathrm{pas}}(\widehat{\mathbf{d}}) \;.$$

The passive stress $\mathbf{P}_{\mathrm{s}}^{\mathrm{pas}}$ accounts for the elastic response through a hyperelastic constitutive law [25, 45, 59], while the active stress $\mathbf{P}_{\mathrm{s}}^{\mathrm{act}}$ takes into account the contractile force [44, 52]. The displacement field $\widehat{\mathbf{d}}$ defines the current configuration of the solid subdomain through

$$\begin{gathered} \boldsymbol{\psi}_{\mathrm{s}}(\widehat{\mathbf{x}}, t) = \widehat{\mathbf{x}} + \widehat{\mathbf{d}}(\widehat{\mathbf{x}}, t) \;, \\ \Omega_{\mathrm{s}} = \left\{ \mathbf{x} \in \mathbb{R}^3 : \mathbf{x} = \boldsymbol{\psi}_{\mathrm{s}}(\widehat{\mathbf{x}}, t),\ \widehat{\mathbf{x}} \in \widehat{\Omega}_{\mathrm{s}} \right\} \;. \end{gathered}$$

Finally, fluid and solid are coupled at their interface Σ by prescribing the continuity of velocity and stress, that is [7, 12]

$$\begin{cases} \mathbf{u} = \dfrac{\partial \mathbf{d}}{\partial t} & \text{on } \Sigma \;, \\ \sigma_{\mathrm{f}}(\mathbf{u}, p)\mathbf{n} = \dfrac{1}{J} \mathbf{F} \mathbf{P}_{\mathrm{s}}(\mathbf{d}, t)^T \mathbf{n} & \text{on } \Sigma \;, \end{cases}$$

where $\widehat{\mathbf{F}} = \mathbf{I} + \boldsymbol{\nabla} \widehat{\mathbf{d}}$, $\widehat{J} = \det \widehat{\mathbf{F}}$, $\mathbf{F}$ and J are their counterparts in the deformed configuration, and $\mathbf{n}$ is the unit vector normal to Σ, outgoing from Ω_{f}.

To close the problem, both the fluid and solid equations are endowed with suitable boundary and initial conditions [13, 25, 63].

2.2. RIIS-mechanics coupling

The resistive terms $\mathbf{R}_k$ in (3) can be interpreted as force densities exerted by the fluid on the valves. Indeed, these forces provide a simplified representation of the interface forces exchanged by blood and valve leaflets. In real hearts, the leaflets are attached to the cardiac walls, to which these forces are transmitted. The model discussed in Section 2.1 neglects this attachment, thus leading to an imbalance of forces in the FSI system. In other words, the system as a whole does not satisfy Newton's laws.

This can lead to unphysical results. Consider, for example, a ventricular chamber during an isovolumetric phase, when both valves are closed. If we assume that the pressure is uniform within the chamber, then the pressure forces that act on the endocardium and on the valves have null resultant, and thus do not lead to a net acceleration of the chamber walls (Figure 1a). This is consistent with the fact that the pressure forces are internal to the FSI system. However, if we apply the model discussed in Section 2.1, the forces exterted by the fluid on the valve leaflets do not act on the solid, and the remaining pressure forces acting on the chamber walls now have a non-zero resultant (Figure 1b). This may lead to an acceleration of the FSI system, even though there are no external forces acting on it. This imbalance is also present if the pressure is not homogeneous within the chamber. We demonstrate this behavior in Section 3.

To address this issue, we modify the solid mechanics equation (4) by adding a distributed force $\widehat{\mathbf{g}} : \widehat{\Omega}_{\mathrm{s}} \times (0, T) \to \mathbb{R}^3$, accounting for the attachment forces between the valves and the walls:

$$\begin{gathered} \rho_{\mathrm{s}} \frac{\partial^2 \widehat{\mathbf{d}}}{\partial t^2} - \boldsymbol{\nabla} \cdot \mathbf{P}_{\mathrm{s}}(\widehat{\mathbf{d}}, t) = \widehat{J} \widehat{\mathbf{g}} \;, \\ \widehat{\mathbf{g}}(\widehat{\mathbf{x}}, t) = \sum_{k=1}^{N_{\mathrm{v}}} \widehat{\mathbf{g}}_k(\widehat{\mathbf{x}}, t) \;. \end{gathered}$$

To derive an expression for the forces $\widehat{\mathbf{g}}_k$, we make the following assumptions.

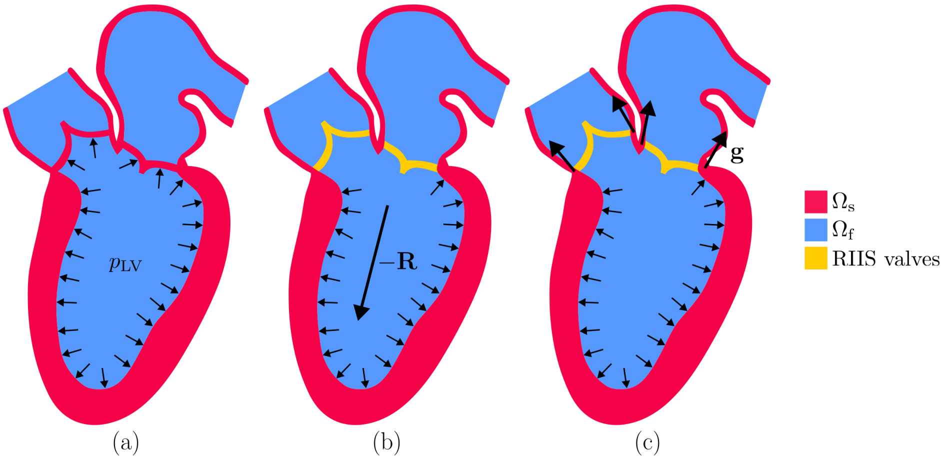

(a) (b) (c)

Figure 1: (a) When valves are attached to the wall, the resultant of pressure forces is zero (assuming that the pressure is constant within the chamber). (b) If the valves are represented through RIIS, the forces they are subject to do not transfer to the wall, and thus the forces acting on the wall have a non-zero resultant. (c) Including the forces $\mathbf{g}$ to account for the attachment of valves to the wall, the equilibrium is restored.

Assumption 1. In the deformed configuration, each surface Γ_k is in contact with the structure domain, that is $\Gamma_k \cap \Omega_{\mathrm{s}} \neq \varnothing$.

Assumption 2. Each valve remains in equilibrium at all times, meaning the net force acting on it is zero.

Assumption 3. The spatial distribution of the force $\widehat{\mathbf{g}}_k$ is the same as in the fluid, that is

$$\widehat{\mathbf{g}}_k = \mathbf{C}_k(t)\delta_k(\varphi_k(\widehat{\mathbf{x}} + \widehat{\mathbf{d}}))\ .$$

Notice that this is different from zero owing to Assumption 1.

By Assumption 2, we choose $\mathbf{C}_k(t)$ such that, at every time t, the resultant of $\widehat{\mathbf{g}}_k$ equals the force that the fluid exerts on the k-th valve, denoted by $\mathbf{F}_k$:

$$\mathbf{F}_k(t) = \int_{\Omega_{\mathrm{s}}} \mathbf{g}_k \,\mathrm{d}\mathbf{x} = \int_{\widehat{\Omega}_{\mathrm{s}}} \widehat{J}\widehat{\mathbf{g}}_k \,\mathrm{d}\widehat{\mathbf{x}} = \mathbf{C}_k(t) \int_{\widehat{\Omega}_{\mathrm{s}}} \widehat{J}\delta_k(\varphi_k(\widehat{\mathbf{x}} + \widehat{\mathbf{d}}))\,\mathrm{d}\widehat{\mathbf{x}}\ .$$

Introducing

$$V_k(t) = \int_{\widehat{\Omega}_{\mathrm{s}}} \widehat{J}\delta_k(\varphi_k(\widehat{\mathbf{x}} + \widehat{\mathbf{d}}))\,\mathrm{d}\widehat{\mathbf{x}}\ ,$$

we obtain:

$$\mathbf{C}_k(t) = \frac{\mathbf{F}_k(t)}{V_k(t)}\ ,$$

$$\widehat{\mathbf{g}}_k(\widehat{\mathbf{x}}, t) = \frac{\mathbf{F}_k(t)}{V_k(t)}\delta_k(\varphi_k(\widehat{\mathbf{x}} + \widehat{\mathbf{d}}))\ .$$

Notice that $V_k(t) > 0$ for all $t > 0$ by Assumption 1.

The forces $\mathbf{F}_k(t)$ are readily computed by integrating the resistive term of Navier-Stokes momentum equation:

$$\mathbf{F}_k(t) = \int_{\Omega_{\mathrm{f}}} \mathbf{R}_k(\mathbf{u}, \mathbf{u}_{\mathrm{ALE}})\,\mathrm{d}\mathbf{x}\ .$$

With a slight abuse of notation, we will henceforth denote the forces acting on the solid with $\widehat{\mathbf{g}}(\mathbf{d}, \mathbf{u}, t)$ and $\widehat{\mathbf{g}}_k(\mathbf{d}, \mathbf{u}, t)$, to emphasize their dependence on the solid displacement (and its derivatives) and on the fluid velocity.

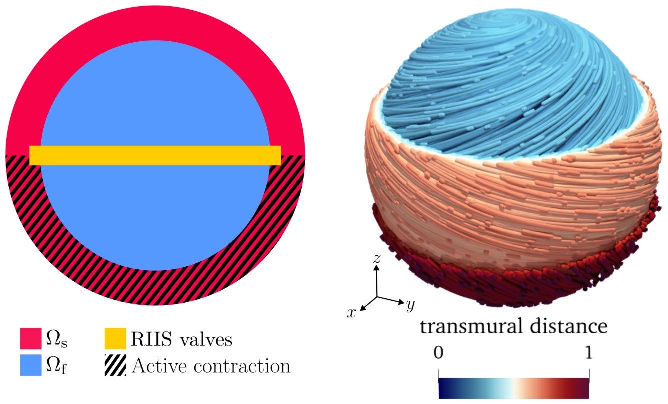

(a) (b)

Figure 2: Idealized spherical benchmark (Section 3.1). (a) Schematic representation of the domain. (b) Streamline representation of the fiber field, colored according to the transmural distance. We show clipped layers of the solid domain for clarity.

2.3. Valve-wall coupling in electromechanical models

It is worth observing that issues in the balance of the pressure forces acting in chamber walls may also arise in models of cardiac electromechanics, that is models in which hemodynamics is surrogated with lumped-parameters circulation models. For ventricular models where the domain is artificially cut at the base of the ventricle, this can be addressed by the so-called energy-consistent boundary conditions [43, 45], which make sure that the boundary forces exerted on the ventricular base balance the pressure forces acting on the walls. Alternatively, the force balance can be ensured by adding solid discs in place of the valves [6, 25, 31, 53, 54]. These, however, are not practical for models involving three-dimensional fluid dynamics. The model proposed in this work can be seen as an extension of these techniques to FSI models.

2.4. Discretization and solvers

We introduce a partition of the time domain $(0, T)$ into intervals (t^n, t^{n+1}), where $t^n = n\Delta t$, with $\Delta t > 0$ the time discretization step. We denote with a superscript n the time-discrete approximation of a function at time t^n, e.g. $\mathbf{u}^n \approx \mathbf{u}(t^n)$. We approximate time derivatives through first-order finite difference formulas. To address the coupling of fluid displacement, fluid and solid, we consider the geometrically-explicit monolithic scheme discussed in [12], suitably adapted to account for resistive modeling of valves.

The newly added term $\widehat{\mathbf{g}}$ is nonlinear with respect to the solid displacement $\mathbf{d}$, and it introduces a further source of fluid-solid coupling in the problem, through the dependency of the force density $\widehat{\mathbf{g}}$ on the fluid velocity $\mathbf{u}$ in the vicinity of the immersed surfaces. For its numerical discretization, we use an explicit treatment, that is we compute the valve forces using the fluid velocity, pressure and solid displacement from previous time step. This facilitates the convergence of the nonlinear solver, without causing instability in our numerical experiments (see Section 3). We remark that this choice introduces an error of the first order with respect to the time step size Δt, which might hinder the accuracy of higher order time discretization schemes. This limitation can be overcome by using a suitable higher-order extrapolation in computing $\widehat{\mathbf{g}}$.

Test case	**Mesh**	**# elements**	**# nodes**	$h_{\min}$[mm]	h_{avg}[mm]	$h_{\max}$[mm]
sphere	fluid	1 154 477	196 239	0.492	0.829	1.140
	solid	1 171 822	218 394	0.481	0.816	1.137
heart	fluid	1 306 215	225 801	0.513	1.487	4.031
	solid	790 901	158 877	0.341	1.343	3.241

Table 1: Number of elements, nodes, and minimum, average and maximum element diameter for the meshes used in this work. All meshes are tetrahedral. The sphere meshes were generated using `gmsh` [32], while the heart meshes were generated with VMTK [34] and the techinques discussed in [26].

The resulting time discrete problem reads:

$$
\begin{cases}
\mathcal{L}_{\mathrm{ALE}}(\widehat{\mathbf{d}}_{\mathrm{ALE}}^{n+1}) = \mathbf{0} & \text{in } \widehat{\Omega}_{\mathrm{f}}\,, \\
\widehat{\mathbf{d}}_{\mathrm{ALE}}^{n+1} = \widehat{\mathbf{d}}^{n} & \text{on } \widehat{\Sigma}\,, \\
\widehat{\mathbf{d}}_{\mathrm{ALE}}^{n+1} = \mathbf{0} & \text{on } \partial\widehat{\Omega}_{\mathrm{f}}\backslash\widehat{\Sigma}\,, \\
\widehat{\mathbf{u}}_{\mathrm{ALE}}^{n+1} = \dfrac{\widehat{\mathbf{d}}_{\mathrm{ALE}}^{n+1} - \widehat{\mathbf{d}}_{\mathrm{ALE}}^{n}}{\Delta t} & \text{in } \widehat{\Omega}_{\mathrm{f}} \\[3ex]
\rho_{\mathrm{f}}\dfrac{\mathbf{u}^{n+1} - \mathbf{u}^{n}}{\Delta t} + \rho_{\mathrm{f}}\left((\mathbf{u}^{n} - \mathbf{u}_{\mathrm{ALE}}^{n+1}) \cdot \boldsymbol{\nabla}\right)\mathbf{u}^{n+1} & \\
\qquad - \boldsymbol{\nabla} \cdot \sigma_{\mathrm{f}}(\mathbf{u}^{n+1}, p^{n+1}) + \mathbf{R}(\mathbf{u}^{n+1}, \mathbf{u}_{\mathrm{ALE}}^{n+1}) = \mathbf{0} & \text{in } \Omega_{\mathrm{f}}^{n+1}\,, \\
\boldsymbol{\nabla} \cdot \mathbf{u}^{n+1} = 0 & \text{in } \Omega_{\mathrm{f}}^{n+1}\,, \\[3ex]
\rho_{\mathrm{s}}\dfrac{\widehat{\mathbf{d}}^{n+1} - 2\widehat{\mathbf{d}}^{n} + \widehat{\mathbf{d}}^{n-1}}{\Delta t^2} - \boldsymbol{\nabla} \cdot \mathbf{P}_{\mathrm{s}}(\widehat{\mathbf{d}}^{n+1}, \widehat{\mathbf{s}}^{n+1}) = \widehat{J}^{n}\widehat{\mathbf{g}}(\widehat{\mathbf{d}}^{n}, \mathbf{u}^{n}, t^{n}) & \text{in } \widehat{\Omega}_{\mathrm{s}}\,, \\[3ex]
\mathbf{u}^{n+1} = \dfrac{\mathbf{d}^{n+1} - \mathbf{d}^{n}}{\Delta t} & \text{on } \Sigma^{n+1}\,, \\
\sigma_{\mathrm{f}}(\mathbf{u}^{n+1}, p^{n+1})\mathbf{n}^{n+1} = \dfrac{1}{J^{n+1}}F^{n+1}\mathbf{P}_{\mathrm{s}}(\mathbf{d}^{n+1}, \mathbf{s}^{n+1})^{T}\mathbf{n}^{n+1} & \text{on } \Sigma^{n+1}\,,
\end{cases}
$$

endowed with appropriate boundary and initial conditions for both fluid and solid.

Finally, the problem is discretized in space using finite elements, with piecewise linear polynomials on a tetrahedral mesh, for all the problems involved. Navier-Stokes equations are stabilized using the VMS-LES method [28], modified to account for the presence of the resistive term **R** [13, 63]. We linearize the coupled fluid-solid system through Newton's method and then solve it with the preconditioned GMRES method [12]. The models and methods described in this paper were implemented using `life`$^{\mathtt{x}}$[1] [1, 2, 11], a C++ library for the simulation of multiphysics problems for cardiac applications, based on `deal.II`[2] [3, 4].

3. Numerical results

This section presents numerical experiments that demonstrate the effect of the proposed model modification. Table 1 reports details on the meshes used for the numerical experiments. All simulations were performed on the LEONARDO supercomputer made available by CINECA, Italy[3].

---

[1] `https://lifex.gitlab.io`

[2] `https://dealii.org`

[3] Technical specifications: `https://wiki.u-gov.it/confluence/display/SCAIUS/UG3.2%3A+LEONARDO+UserGuide`.

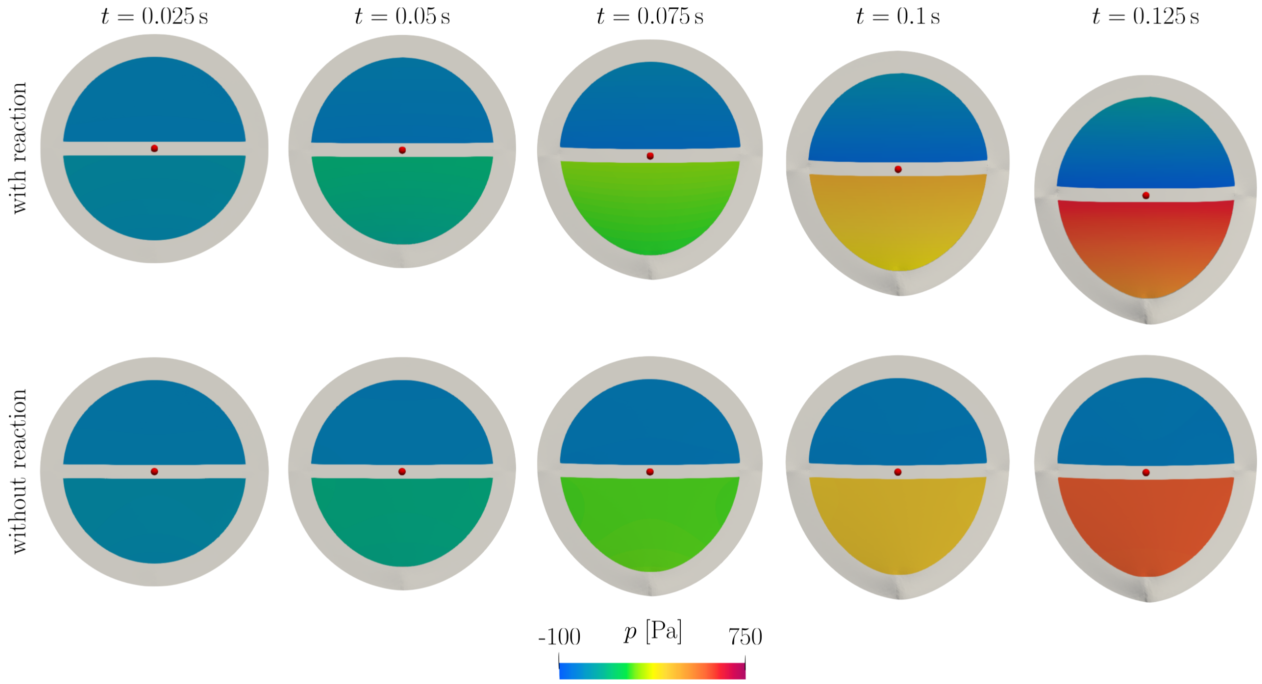

Figure 3: Idealized spherical benchmark (Section 3.1). Evolution over time of the system deformation and fluid pressure, without (top) and with (bottom) the force $\mathbf{g}$. The red dot marks the position of the system's center of mass.

3.1. Idealized spherical benchmark

We consider a geometrically idealized setting in which the fluid domain is a sphere, the structure domain is a spherical shell surrounding it, and a resistive planar surface cuts the domain in half, as depicted in Figure 2a. We assume that the solid follows the transversely isotropic Guccione constitutive law for ventricular tissue [59], with the same coefficients as in [25]. We prescribe a fiber distribution (Figure 2b) that is tangent to the sphere, with transmurally varying orientation, inspired by ventricular fiber generation methods [42]. We prescribe an active contraction in the bottom half of the sphere, with the following expression:

$$\mathbf{P}_\mathrm{s}^\mathrm{act}(\widehat{\mathbf{d}}, t) = \begin{cases} \dfrac{A_\mathrm{max}}{2}\left(1 - \cos\left(\dfrac{\pi t}{T_\mathrm{max}}\right)\right)\dfrac{\widehat{\mathbf{F}}\widehat{\mathbf{f}} \otimes \widehat{\mathbf{f}}}{\|\widehat{\mathbf{F}}\widehat{\mathbf{f}}\|} & \text{if } z \leq 0\,, \\ 0 & \text{otherwise}\,, \end{cases}$$

where $\widehat{\mathbf{f}}$ is the orientation of the fiber field in the undeformed configuration, $A_\mathrm{max} = 5\,\mathrm{kPa}$ is the peak contraction, and $T_\mathrm{max} = 0.25\,\mathrm{s}$ is the time at which that peak occurs. With this choice, the structure contracts in the bottom half, leading to an increase in pressure in the lower chamber, which mimics in this idealized setting the behavior of a ventricle and atrium during ventricular systole. We assume the system to be initially at rest, i.e $\mathbf{u} = \mathbf{0}$, $\widehat{\mathbf{d}} = \mathbf{0}$ and $\frac{\partial \widehat{\mathbf{d}}}{\partial t} = \mathbf{0}$ at time $t = 0$. We impose homogeneous Neumann boundary conditions on the whole external boundary of the solid, that is

$$\mathbf{P}_\mathrm{s}(\widehat{\mathbf{d}}, t)\mathbf{n} = \mathbf{0} \qquad \text{on } \partial\widehat{\Omega}_\mathrm{s} \backslash \widehat{\Sigma}\,.$$

No boundary conditions are needed for the fluid subproblem, since the fluid domain boundary coincides with the fluid-solid interface.

Under these conditions, we expect that the center of mass of the fluid-solid system, initially placed in the origin of the reference system, does not move. Indeed, there are no external forces acting on the system, and the prescribed active contraction gives rise to internal forces whose resultant is null, by Newton's third law.

	without g [s]	**with g** [s]
total time	1693.3	1787.3
linear solver	1518.9	1554.3
fluid assembly	293.6	299.9
solid assembly	219.6	223.1
compute **g**	-	88.5

Table 2: Idealized spherical benchmark (Section 3.1). Breakdown of the simulation wall time, both with and without valve attachment forces $\mathbf{g}$.

The surface cutting the domain in half prevents flow between the upper and lower parts of the fluid domain. Therefore, we expect the pressure to rise in the bottom chamber, due to the contraction, but without any average displacement of the fluid-solid system.

We use a harmonic extension operator to displace the fluid domain [51]. We set the final time to $T = 0.25\,\mathrm{s}$ and, unless otherwise specified, we use a time step size $\Delta t = 5 \cdot 10^{-4}\,\mathrm{s}$. We run simulations in this setting both with and withouth the newly introduced term $\widehat{\mathbf{g}}$.

Figure 3 reports some snapshots of the solution. Figures 4a and 4b plot the evolution of the vertical position and velocity of the center of mass $\overline{\mathbf{x}}$ of the whole fluid-solid system. When the forces $\widehat{\mathbf{g}}$ are not included, the center of mass exhibits a clear downward acceleration, which is unphysical. As discussed in Section 2.2, this happens due to the higher pressure in the bottom chamber not being properly balanced (Figure 4c), and thus accelerating the system downwards.

Conversely, including $\widehat{\mathbf{g}}$ in the solid momentum equation removes this imbalance, thus causing the center of mass to remain stationary. A small downward drift is still observed (Figure 4a), which is due to the explicit time discretization used for $\widehat{\mathbf{g}}$. Indeed, as the time step size Δt is reduced, the spurious drift tends to zero, with approximate order 1, which is consistent with the order of the explicit discretization. We verify this by plotting the vertical position of the center of mass at the final simulation time T with different choices of Δt in Figure 4d.

Table 2 reports a breakdown of the computational cost in the two cases. The computational cost when they are included is only marginally larger than when they are neglected, thanks to the choice of computing the valve forces explicitly. The cost is dominated by the solution of the linear system arising from the discretization of the FSI problem, with the computation of $\widehat{\mathbf{g}}$ being a minor additional cost.

3.2. Realistic left heart model

We consider a cardiac FSI model driven by electrophysiology, adapted from [13]. The domain, depicted in Figure 5, represents a realistic human left heart [66]. With respect to the original publication [13], we replace the monodomain model of cardiac electrophysiology with an eikonal-diffusion model [52], in the interest of computational efficiency. Additionally, we include atrial contraction, which was previously neglected. The model is described in more detail in Appendix A. We set the heartbeat period to $T_{\mathrm{hb}} = 0.8\,\mathrm{s}$.

The model includes two resistive surfaces, to represent the mitral valve (MV) and aortic valve (AV) (Figure A.9). As done in [13, 63], we valves open and close according to the pressure difference between upstream and downstream.

We use a time step size $\Delta t = 2 \cdot 10^{-4}\,\mathrm{s}$. The simulation runs for two heart cycles ($T = 1.6\,\mathrm{s}$), and we report results on the second one, for which the simulation has approximately reached a periodic state. The times reported in this section are relative to the second heartbeat. Figure 6 displays some snapshots of the numerical solution, and Figure 7 reports the traces of pressure and volume in the chambers, as well as the evolution of the force densities $\frac{\mathbf{F}_k}{V_k}$ for the two valves.

The cardiac cycle starts during ventricular diastole, with AV closed and MV open. The atrium contracts around time $t = 100\,\mathrm{ms}$, which is shortly followed by ventricular contraction. This causes the ventricular pressure to rise and the MV to close, beginning isovolumetric contraction.

If we neglect the valve forces, the high ventricular pressure leads to a force that pulls the ventricle in the direction of the apex (as schematized in Figure 1, and visualized in Figure 6). This results in a fast and

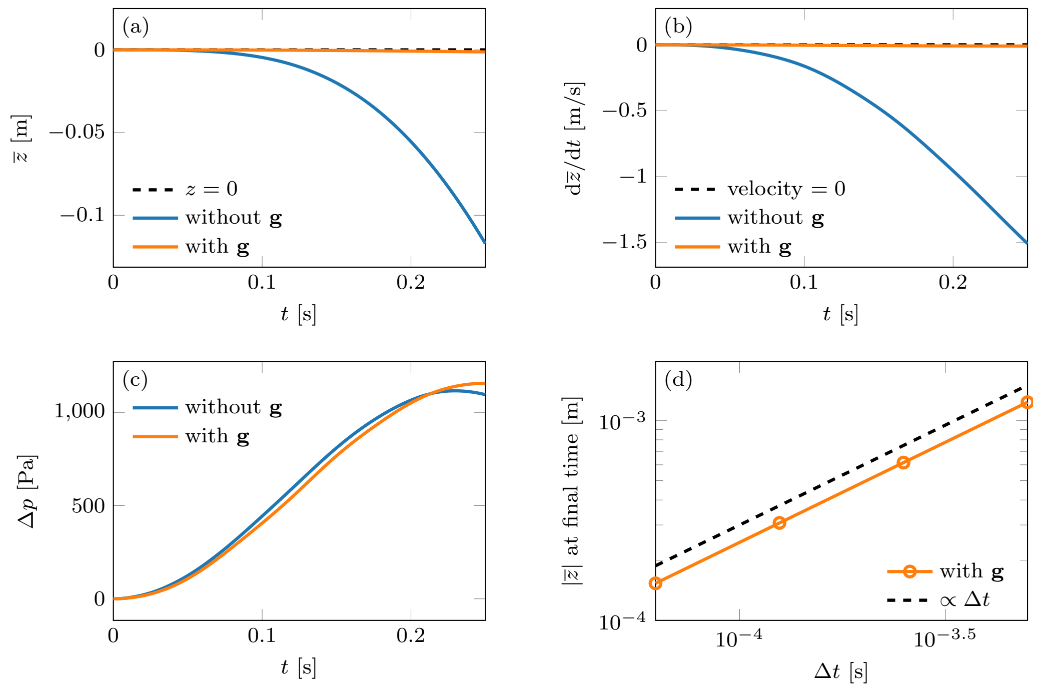

Figure 4: Idealized spherical benchmark (Section 3.1). Unless otherwise stated, the plot are obtained with $\Delta t = 5 \cdot 10^{-4}$ s. (a) Vertical position $\overline{z}$ of the center of mass of the FSI system over time, with and without the attachment force $\mathbf{g}$. (b) Vertical velocity of the center of mass over time, with and without the attachment force $\mathbf{g}$. (c) Pressure jump over time between the lower and upper chambers of the sphere, with and without the attachment force $\mathbf{g}$. (d) Vertical position of the center of mass of the FSI system at the final simulation time, plotted against the time step size Δt. We omit the plot for the case that neglects $\mathbf{g}$, for which the final vertical position is approximately $|\overline{z}| = 1.5 \cdot 10^{-1}$ m for all choices of Δt.

large displacement of the ventricle along its longitudinal axis, which also gives rise to high strains in the atrial wall (Figure 6). Correspondingly, there are strong jets in the pulmonary veins, which are absent if the valve forces are included in the model. This behavior becomes apparent also in pressure and volume traces and in the pressure-volume loops of both atrium and ventricle (Figure 7), which show sharp oscillations at the beginning of the systolic phase. During diastole, due to the atrial and ventricular pressures being approximately equal and the MV being open, the elasticity of the atrium and the pericardial boundary conditions allow the solid to return to its original configuration. As previously discussed, this unphysical behavior arises from an incorrect balance of forces in the FSI system, which is most evident when there are significant differences among the chamber pressures, such as during ventricular systole.

We further remark that the high strains may lead to an unrealistic feedback effect onto the force generation model [44], which is sensitive to both fiber strain and strain rate. Additionally, in more sophisticated models that include detailed mechano-electric feedbacks, such deformations may even trigger abnormal electrical activity [48], thus largely affecting the simulation outcome.

If instead we include the valve forces, we no longer observe any unphysical oscillations in the ventricular displacement, nor in the pressure-volume loops. This is evident in particular in the morphology of the atrial loop, which is much more consistent with physiology if valve forces are included in the model [10, 25, 40].

Figure 8 reports the evolution of the pressure jump between downstream and upstream and of valve force densities $\frac{\mathbf{F}_k}{V_k}$ for the two valves, obtained from the simulation including valve forces. Considering only the closed valve configuration, corresponding to positive pressure jumps, we observe a nearly perfect linear relation between pressure jump and force. The slope of this relation is significantly higher for the MV ($2.5\,\mathrm{N}/(\mathrm{m}^3 \cdot \mathrm{mmHg})$) than it is for the AV ($0.47\,\mathrm{N}/(\mathrm{m}^3 \cdot \mathrm{mmHg})$). We attribute this effect to the different surface areas, curvatures and overall geometry of the two valves in closed configuration (Figure A.9).

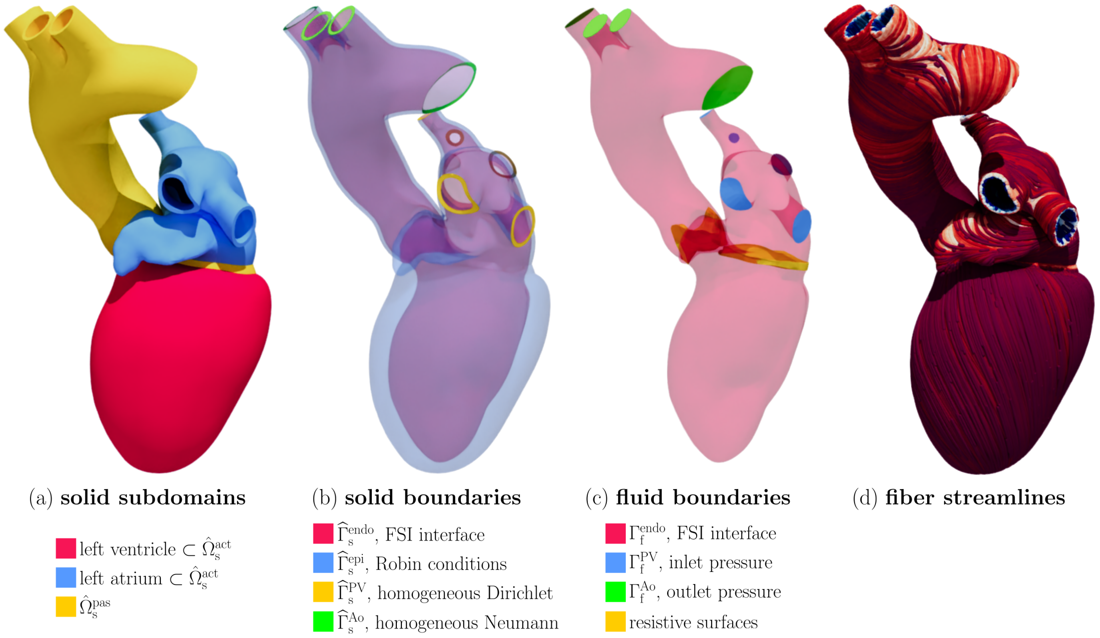
(a) **solid subdomains** (b) **solid boundaries** (c) **fluid boundaries** (d) **fiber streamlines**

Figure 5: Left heart test case. (a) Decomposition of the solid domain $\widehat{\Omega}_s$ into the active part $\widehat{\Omega}_s^{\mathrm{act}}$, including the ventricle and atrium, and the passive part $\widehat{\Omega}_s^{\mathrm{pas}}$, including the aorta and atrioventricular ring. (b) Solid domain boundaries. (c) Fluid domain boundaries. (d) Streamlines of the fiber field $\mathbf{f}$, colored according to the transmural coordinate for readability.

4. Conclusions

This paper introduces an improvement of the RIIS model, allowing it to represent valve leaflets in FSI simulations of the heart, by accounting for the attachment forces exchanged by valves and cardiac walls. These forces are computed in such a way to balance the forces exchanged by the fluid and the valves, thus making sure that the model satisfies Newton's laws. Numerical experiments illustrate the issues arising from a naive application of RIIS in FSI contexts, as well as the improvements obtained by including the proposed modification. A test case using a realistic left heart model highlights how including valve attachment forces is crucial to obtain a physically meaningful behavior of the heart. While the present work focuses on RIIS, the same principles may be straightforwardly extended to other resistive methods for valve modeling, thus providing a general approach to include simplified models of valves in FSI simulations of the heart.

Acknowledgements

The present research is part of the activities of "Dipartimento di Eccellenza 2023–2027", MUR, Italy, Dipartimento di Matematica, Politecnico di Milano. The authors have received support from the project PRIN2022, MUR, Italy, 2023–2025, 202232A8AN "Computational modeling of the heart: from efficient numerical solvers to cardiac digital twins". The authors have received support from the EuroHPC JU project dealii-X (grant number 101172493) funded under the HORIZON-EUROHPC-JU-2023-COE-03-01 initiative. The authors acknowledge their membership to INdAM GNCS - Gruppo Nazionale per il Calcolo Scientifico (National Group for Scientific Computing, Italy). The authors acknowledge the INdAM GNCS project CUP E53C23001670001. The authors acknowledge the CINECA award under the ISCRA initiative, for the availability of high performance computing resources and support.

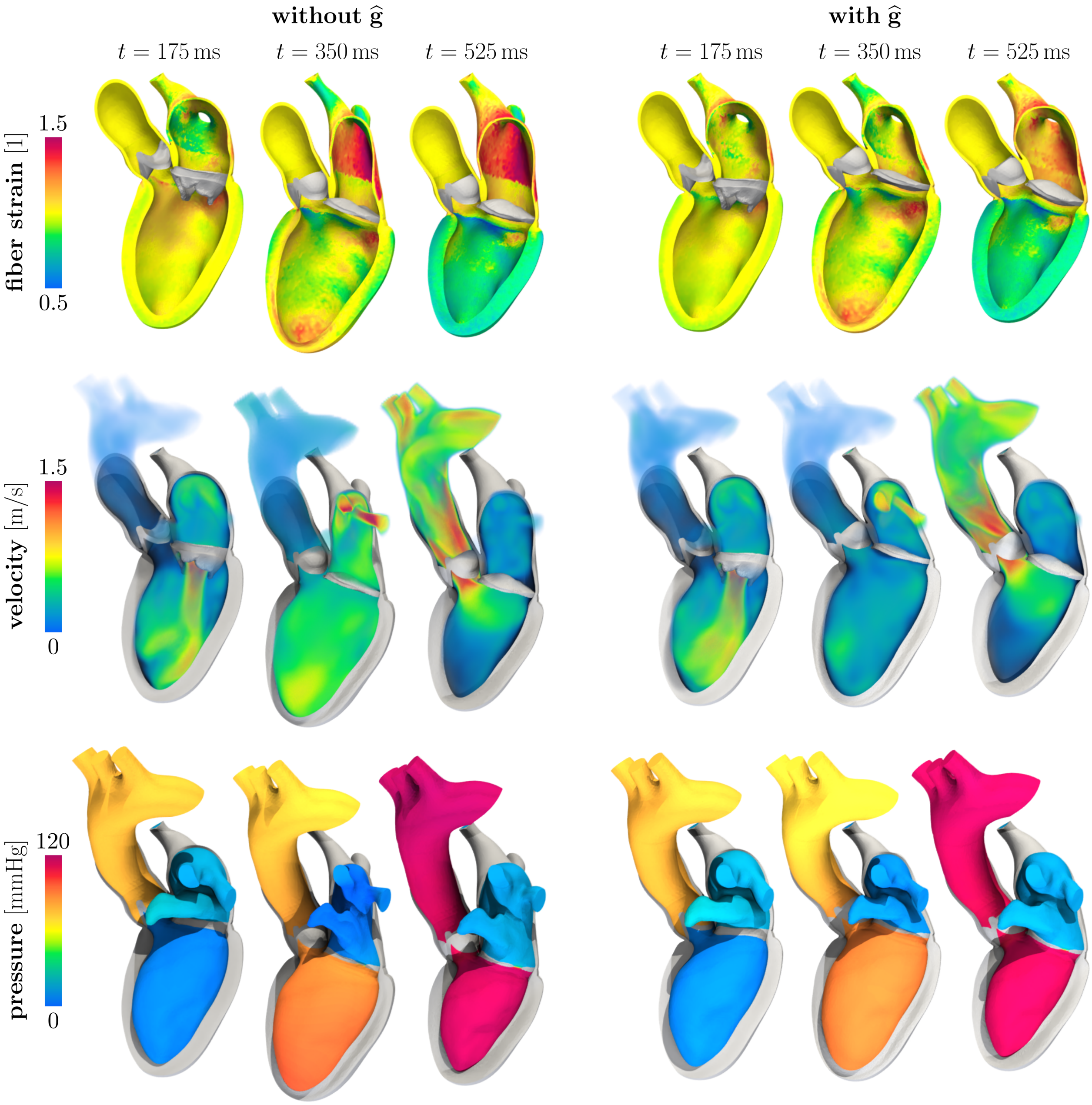

Figure 6: Left heart test case. Snapshots of the numerical solution without (left) and with (right) the valve forces $\widehat{\mathbf{g}}$. We report the strain along fibers $\|\widehat{\mathbf{F}}\widehat{\mathbf{f}}\|$ (top), a volume rendering of the fluid velocity $\mathbf{u}$ (middle) and the pressure p (bottom). The domain is represented in the deformed configuration. For each, we report a frame during diastolic filling ($t = 175\,\text{ms}$), one during isovolumetric contraction ($t = 350\,\text{ms}$) and one during ejection ($t = 525\,\text{ms}$).

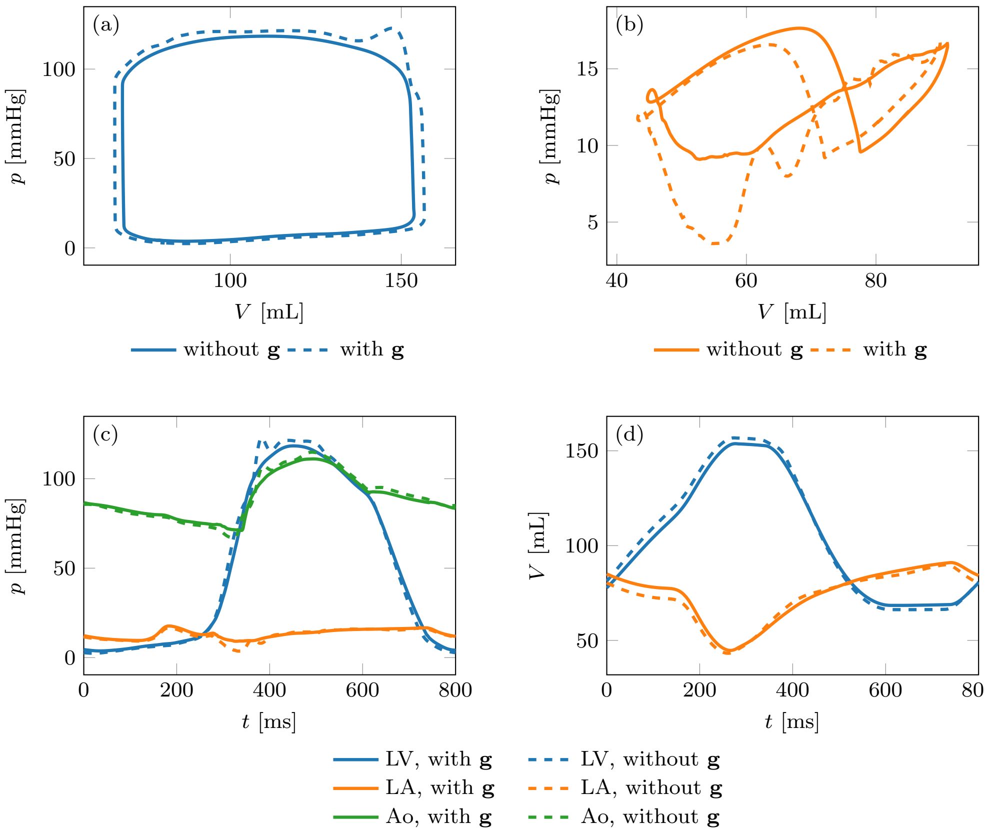

Figure 7: Left heart test case. (a) Left ventricular pressure-volume loop. (b) Left atrial pressure-volume loop. (c) Traces of pressure in the ventricle (LV), atrium (LA) and ascending aorta (Ao) over time. (d) Traces of volume of the ventricular and atrial chamber over time. In all the plots, the solid lines correspond to the simulation including valve forces, and the dashed lines to the simulation neglecting them.

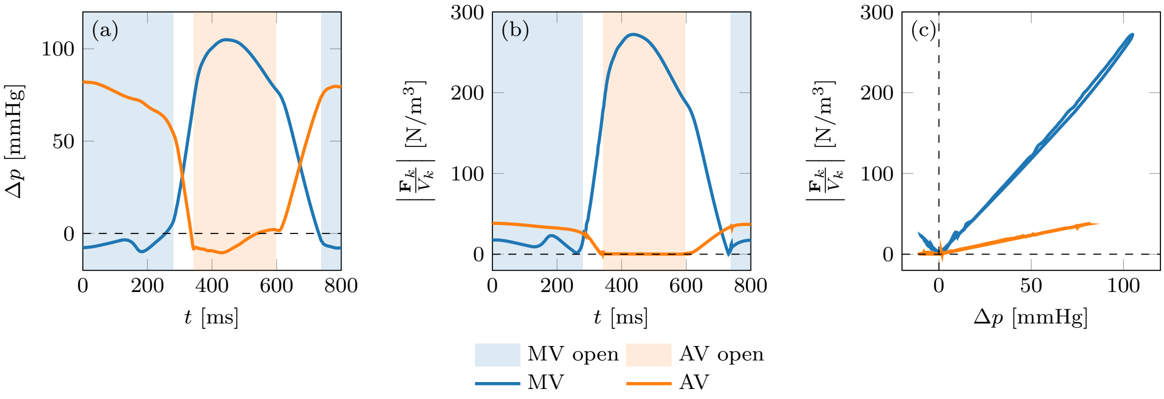

Figure 8: Left heart test case, including valve forces $\widehat{\mathbf{g}}$. (a) Pressure jump between downstream and upstream over time for each valve, i.e. $\Delta p = p_{\text{down}} - p_{\text{up}}$. (b) Magnitude of the force density $\frac{\mathbf{F}_k}{V_k}$ over time for the two valves. (c) Magnitude of the force density plotted against the pressure jump for the two valves. Shaded areas in plots (a) and (b) highlight times during which one of the valves is open.

Figure A.9: Left heart test case. Closeup visualization of the AV (red) and MV (yellow) in their closed configuration at the beginning of the simulation.

Appendix A. Left heart eikonal-mechanics-fluid model

We partition the solid domain into an electrically active part $\widehat{\Omega}_\mathrm{s}^\mathrm{act}$ and a passive part $\widehat{\Omega}_\mathrm{s}^\mathrm{pas}$, such that $\widehat{\Omega}_\mathrm{s} = \widehat{\Omega}_\mathrm{s}^\mathrm{act} \cup \widehat{\Omega}_\mathrm{s}^\mathrm{pas}$. The active part includes the left ventricle and left atrium, whereas the passive part includes the atrioventricular ring and the ascending aorta. Additionally, we denote by $\widehat{\Gamma}_\mathrm{s}^\mathrm{epi}$ the epicardial boundary of the structure subdomain, by $\widehat{\Gamma}_\mathrm{s}^\mathrm{PV}$ the pulmonary vein inlet sections, and by $\widehat{\Gamma}_\mathrm{s}^\mathrm{Ao}$ the aorta outlet sections. Similarly, $\widehat{\Gamma}_\mathrm{f}^\mathrm{PV}$ and $\widehat{\Gamma}_\mathrm{f}^\mathrm{Ao}$ denote the inlet and outlet boundaries of the fluid subdomain.

Fibers are generated by adapting the method presented in [25], by restricting the whole-heart fibers to the left heart geometry considered here. This defines an orthonormal triplet $\{\widehat{\mathbf{f}}, \widehat{\mathbf{s}}, \widehat{\mathbf{n}}\}$ at every point of the domain [42].

We define the contraction of the muscle through the eikonal-mechanics framework previously described in [52]. To this end, prior to the FSI simulation, we solve the following eikonal-diffusion problem in the active solid subdomain:

$$\begin{cases} c_0 \sqrt{\boldsymbol{\nabla}\varphi \cdot \mathbf{D}\boldsymbol{\nabla}\varphi} - \boldsymbol{\nabla} \cdot (\mathbf{D}\boldsymbol{\nabla}\varphi) = 1 & \text{in } \widehat{\Omega}_\mathrm{s}^\mathrm{act} \,, \\ \varphi = \varphi_0 & \text{in } \widehat{S} \subset \widehat{\Omega}_\mathrm{s}^\mathrm{act} \,, \\ (\boldsymbol{\Sigma}\boldsymbol{\nabla}\varphi) \cdot \mathbf{n} = 0 & \text{on } \partial\widehat{\Omega}_\mathrm{s}^\mathrm{act} \backslash \widehat{S} \,, \end{cases} \tag{A.1}$$

where $\varphi : \widehat{\Omega}_\mathrm{s}^\mathrm{act} \to [0, T_\mathrm{hb})$ is the activation time, that is the time at which points in the active subdomain are reached by the excitation front, and $T_\mathrm{hb} > 0$ is the heartbeat period. The diffusion tensor $\mathbf{D}$ is defined by

$$\mathbf{D} = \sigma_\mathrm{f} \widehat{\mathbf{f}} \otimes \widehat{\mathbf{f}} + \sigma_\mathrm{s} \widehat{\mathbf{s}} \otimes \widehat{\mathbf{s}} + \sigma_\mathrm{n} \widehat{\mathbf{n}} \otimes \widehat{\mathbf{n}} \,.$$

Following [52], we solve problem (A.1) through a pseudo-time algorithm. Notice that by solving (A.1) only on the active subdomain $\widehat{\Omega}_\mathrm{s}^\mathrm{act}$, we model the fact that the passive subdomain acts as an electrical insulant between atrium and ventricle [25]. The parameters for the eikonal-diffusion model are reported in Table A.3.

Independently, we solve a system of ordinary differential equations (ODEs) representing the ionic activity of a single cell:

$$\begin{cases} \dfrac{\mathrm{d}\mathbf{w}}{\mathrm{d}t} = \mathbf{F}_\mathrm{ion}(\mathbf{w}, u) & \text{in } (0, T) \,, \\ \dfrac{\mathrm{d}u}{\mathrm{d}t} + I_\mathrm{ion}(\mathbf{w}, u) = I_\mathrm{app}(t) & \text{in } (0, T) \,, \\ \mathbf{w}(0) = \mathbf{w}_0 \,, \end{cases}$$

where $\mathbf{w} : [0, T) \to \mathbb{R}^{N_\mathrm{ion}}$ is a vector of ionic state variables. We solve the ionic model for 1000 heartbeat cycles, and then extract the evolution of the intracellular calcium concentration at the last cycle, denoted by $[\mathrm{Ca}^{2+}]_\mathrm{i}^0(t) : [0, T_\mathrm{hb}) \to \mathbb{R}$. We consider the model by ten Tusscher and Panfilov [55] for ventricular tissue and the one by Courtemanche, Ramirez and Nattel [17] for atrial tissue. Finally, we combine the activation time and the calcium transient to compute the evolution of intracellular calcium at every point of the domain:

$$[\mathrm{Ca}^{2+}]_\mathrm{i}(\mathbf{x}, t) = [\mathrm{Ca}^{2+}]_\mathrm{i}^0((t \bmod T_\mathrm{hb}) - \varphi(\mathbf{x})) \qquad \mathbf{x} \in \widehat{\Omega}_\mathrm{s}^\mathrm{act}\ , t \in (0, T)\ ,$$

where $a \bmod b$ denotes the remainder of the division between a and b, that is $a \bmod b = a - b\left\lfloor \frac{a}{b} \right\rfloor$. In other words, the calcium transient is repeated periodically at every point, with period T_hb, and shifted by the activation time φ.

The generation of contractile force in the muscle is regulated by the RDQ20-MF model [25, 44, 63], which is expressed by the following system

$$\frac{\partial \mathbf{s}}{\partial t} = \mathbf{F}_\mathrm{act}\left([\mathrm{Ca}^{2+}]_\mathrm{i}, \mathrm{SL}, \frac{\partial \mathrm{SL}}{\partial t}\right) \qquad \text{in } \widehat{\Omega}_\mathrm{s}^\mathrm{act} \times (0, T)\ ,$$

where $\mathrm{SL} = \mathrm{SL}_0 \, \|\widehat{\mathbf{F}}\widehat{\mathbf{f}}\|$ is the sarcomere length. Table A.4 reports the values of the RDQ20-MF model parameters. The active stress tensor is then defined as

$$\mathbf{P}_\mathrm{s}^\mathrm{act}(\widehat{\mathbf{d}}, t) = T^\mathrm{act}(\mathbf{s}) \left(n_\mathrm{f} \frac{\widehat{\mathbf{F}}\widehat{\mathbf{f}} \otimes \widehat{\mathbf{f}}}{\|\widehat{\mathbf{F}}\widehat{\mathbf{f}}\|} + n_\mathrm{n} \frac{\widehat{\mathbf{F}}\widehat{\mathbf{n}} \otimes \widehat{\mathbf{n}}}{\|\widehat{\mathbf{F}}\widehat{\mathbf{f}}\|} \right)\ ,$$

with T^act defined as in [44]. In the passive subdomain $\widehat{\Omega}_\mathrm{s}^\mathrm{pas}$, the active stress tensor is set to zero.

Concerning passive stress, we use the Guccione model for atrial and ventricular tissue [59], and a neo Hooke model for the atrioventricular ring and for the aortic wall, as done in [13, 25]. The interface between different material models is smoothed as discussed in [13]. The evolution of wall displacement is regulated by the elastodynamics equation (4). We impose homogeneous Dirichlet boundary conditions on the pulmonary vein sections $\widehat{\Gamma}_\mathrm{s}^\mathrm{PV}$, homogeneous Neumann conditions on the aortic sections $\widehat{\Gamma}_\mathrm{s}^\mathrm{Ao}$, and normal viscoelastic Robin conditions on the epicardial boundary $\widehat{\Gamma}_\mathrm{s}^\mathrm{epi}$ (Figure 5b), that is:

$$\begin{cases} \mathbf{d} = \mathbf{0} & \text{on } \widehat{\Gamma}_\mathrm{s}^\mathrm{PV}\ , \\ \mathbf{P}_\mathrm{s}(\mathbf{d}, t)\mathbf{n} = \mathbf{0} & \text{on } \widehat{\Gamma}_\mathrm{s}^\mathrm{Ao}\ , \\ \mathbf{P}_\mathrm{s}(\mathbf{d}, t)\mathbf{n} = -(\mathbf{n} \otimes \mathbf{n}) \left(K_\mathrm{epi}\mathbf{d} + C_\mathrm{epi}\dfrac{\partial \mathbf{d}}{\partial t} \right) & \text{on } \widehat{\Gamma}_\mathrm{s}^\mathrm{epi}\ , \end{cases}$$

where K_epi and C_epi are the positive stiffness and damping coefficients, respectively. Following [25], we use two different sets of coefficients to distinguish between regions in contact with the pericardial sac and regions covered by epicardial fat. We report the parameters for the solid mechanics model in Table A.6.

The fluid domain displacement is computed through a neo-Hooke material law, that is

$$\begin{aligned} \mathcal{L}_\mathrm{ALE}(\widehat{\mathbf{d}}_\mathrm{ALE}) &= \boldsymbol{\nabla} \cdot \mathbf{P}_\mathrm{ALE}(\widehat{\mathbf{d}}_\mathrm{ALE})\ , \\ \mathbf{P}_\mathrm{ALE}(\widehat{\mathbf{d}}_\mathrm{ALE}) &= \mu_\mathrm{ALE}\widehat{J}_\mathrm{ALE}^{-\frac{2}{3}} \left(\widehat{\mathbf{F}}_\mathrm{ALE} - (\widehat{\mathbf{F}}_\mathrm{ALE} : \widehat{\mathbf{F}}_\mathrm{ALE})\widehat{\mathbf{F}}_\mathrm{ALE}^{-1} \right) + \kappa_\mathrm{ALE}\widehat{\mathbf{F}}_\mathrm{ALE}^{-1}\ , \\ \widehat{\mathbf{F}}_\mathrm{ALE} &= \mathbf{I} + \boldsymbol{\nabla}\widehat{\mathbf{d}}_\mathrm{ALE}\ , \\ \widehat{J}_\mathrm{ALE} &= \det \widehat{\mathbf{F}}_\mathrm{ALE}\ , \end{aligned}$$

where μ_ALE and κ_ALE are the stiffness and bulk modulus of the fictitious material representing the fluid domain.

Blood dynamics is modeled through Navier-Stokes equations (1) in ALE reference. We include two resistive surfaces to represent the MV and AV. The displacements mapping the closed configuration onto the open one are derived through rule-based procedures [65]. For each valve, the opening and closing is triggered by the pressure jump between upstream and downstream [13, 63]. Table A.5 reports the parameters for the fluid model, including those for domain displacement and for RIIS.

Subdomain	Parameter	Description	Value	Unit
all	c_0	depolarization velocity	60	$1/\mathrm{s}^{1/2}$
left ventricle	σ_f	fiber conductivity	$1.00 \cdot 10^{-4}$	$\mathrm{m/s^2}$
	σ_s	sheet conductivity	$0.44 \cdot 10^{-4}$	$\mathrm{m/s^2}$
	σ_n	normal conductivity	$0.44 \cdot 10^{-4}$	$\mathrm{m/s^2}$
left atrium	σ_f	fiber conductivity	$7.00 \cdot 10^{-4}$	$\mathrm{m/s^2}$
	σ_s	sheet conductivity	$1.41 \cdot 10^{-4}$	$\mathrm{m/s^2}$
	σ_n	normal conductivity	$1.41 \cdot 10^{-4}$	$\mathrm{m/s^2}$

Table A.3: Left heart test case. Parameters for the eikonal-diffusion model.

At the inlet boundaries $\Gamma_\mathrm{f}^\mathrm{PV}$ and at the outlet boundaries $\Gamma_\mathrm{f}^\mathrm{Ao}$, the fluid model is coupled to a closed-loop, lumped parameter model of the circulatory system [13, 25, 63]. The coupling is expressed by imposing pressure conditions at the inlet and outlet boundaries, where the pressure values are solutions to the circulation model. The flowrates measured at the inlet and outlet sections of the fluid dynamics model are then used as boundary conditions for the circulation model. The parameters for the circulation model are reported in Table A.7.

For additional details on the model and on the numerical methods used for its solution, we refer to [12, 13, 52].

Bibliography

[1] P. C. Africa. lifex: A flexible, high performance library for the numerical solution of complex finite element problems. *SoftwareX*, 20:101252, 2022.

[2] P. C. Africa, I. Fumagalli, M. Bucelli, A. Zingaro, M. Fedele, L. Dede', and A. Quarteroni. lifex-cfd: An open-source computational fluid dynamics solver for cardiovascular applications. *Computer Physics Communications*, 296:109039, 2024.

[3] D. Arndt, W. Bangerth, D. Davydov, T. Heister, L. Heltai, M. Kronbichler, M. Maier, J. Pelteret, B. Turcksin, and D. Wells. The `deal.II` finite element library: design, features, and insights. *Computers & Mathematics with Applications*, 81:407–422, 2021.

[4] D. Arndt, W. Bangerth, M. Feder, M. Fehling, R. Gassmöller, T. Heister, L. Heltai, M. Kronbichler, M. Maier, P. Munch, J.-P. Pelteret, S. Sticko, B. Turcksin, and D. Wells. The `deal.II` library, version 9.4. *Journal of Numerical Mathematics*, 30(3):231–246, 2022.

[5] M. Astorino, J. Hamers, S. C. Shadden, and J.-F. Gerbeau. A robust and efficient valve model based on resistive immersed surfaces. *International Journal for Numerical Methods in Biomedical Engineering*, 28(9):937–959, 2012.

[6] C. M. Augustin, M. A. Gsell, E. Karabelas, E. Willemen, F. W. Prinzen, J. Lumens, E. J. Vigmond, and G. Plank. A computationally efficient physiologically comprehensive 3D–0D closed-loop model of the heart and circulation. *Computer methods in applied mechanics and engineering*, 386:114092, 2021.

[7] Y. Bazilevs, K. Takizawa, and T. E. Tezduyar. *Computational fluid-structure interaction: methods and applications*. John Wiley & Sons, 2013.

[8] L. Bennati, V. Giambruno, F. Renzi, V. Di Nicola, C. Maffeis, G. Puppini, G. B. Luciani, and C. Vergara. Turbulent blood dynamics in the left heart in the presence of mitral regurgitation: a computational study based on multi-series cine-MRI. *Biomechanics and Modeling in Mechanobiology*, 22(6):1829–1846, 2023.

Subdomain	Parameter	Description	Value	Unit
left ventricle	SL_0	sarcomere slack length	2.2	µm
	K_{d0}	dissociation constant	0.36	µM
	α_{Kd}	dissociation constant sensitivity	-0.2083	µM/µm
	μ		10	-
	γ		30	-
	K_{off}	troponin dissociation rate	8	1/s
	K_{basic}	tropomyosin reaction rate	4	1/s
	r_0	crossbridge attachment-detatchment rate	134.31	1/s
	α	crossbridge detachment rate sensitivity	25.184	-
	$\mu_{0,\mathrm{fP}}$	zero-th moment of attached rate	32.225	1/s
	$\mu_{1,\mathrm{fP}}$	first moment of attached rate	0.768	1/s
	a_{XB}	crossbridge stiffness	500	MPa
left atrium	SL_0	sarcomere slack length	1.9	µm
	K_{d0}	dissociation constant	0.865	µM
	α_{Kd}	dissociation constant sensitivity	-1.25	µM/µm
	μ		10	-
	γ		20	-
	K_{off}	troponin dissociation rate	180	1/s
	K_{basic}	tropomyosin reaction rate	20	1/s
	r_0	crossbridge attachment-detatchment rate	134.31	1/s
	α	crossbridge detachment rate sensitivity	25.184	-
	$\mu_{0,\mathrm{fP}}$	zero-th moment of attached rate	32.235	1/s
	$\mu_{1,\mathrm{fP}}$	first moment of attached rate	0.768	1/s
	a_{XB}	crossbridge stiffness	200	MPa

Table A.4: Left heart test case. Parameters for the RDQ20-MF force generation model. If not reported, the parameter values are those presented in the original paper [44].

Submodel Parameter	Description	Value	Unit	
Navier-Stokes	ρ_{f}	fluid density	$1.06 \cdot 10^3$	$\mathrm{kg/m^3}$
	μ	fluid viscosity	$3.5 \cdot 10^{-3}$	$\mathrm{Pa \cdot s}$
RIIS	$\varepsilon_{\mathrm{AV}}$, $\varepsilon_{\mathrm{MV}}$	valve half-thickness	1.5	mm
	R_{AV}, R_{MV}	valve resistances	10^4	$\mathrm{kg/(m \cdot s)}$
	$\Delta t_{\mathrm{MV}}^{\mathrm{open}}$	MV opening ramp duration	10	ms
	$\Delta t_{\mathrm{MV}}^{\mathrm{close}}$	MV closing ramp duration	35	ms
	$\Delta t_{\mathrm{AV}}^{\mathrm{open}}$	AV opening ramp duration	10	ms
	$\Delta t_{\mathrm{AV}}^{\mathrm{close}}$	AV closing ramp duration	80	ms
domain displacement	μ_{ALE}	fluid domain stiffness	0.01	Pa
	κ_{ALE}	fluid domain bulk modulus	0.01	Pa

Table A.5: Left heart test case. Parameters for the fluid dynamics model.

Subdomain	**Parameter**	**Description**	**Value**	**Unit**
	ρ_s	solid density	10^3	$\mathrm{kg/m^3}$
	b_f	Guccione fiber parameter	8	-
	b_s	Guccione sheet parameter	6	-
	b_n	Guccione normal parameter	3	-
	b_fs	Guccione fiber-sheet parameter	12	-
	b_fn	Guccione fiber-normal parameter	3	-
	b_sn	Guccione sheet-normal parameter	3	-
	κ_G	Guccione bulk modulus	$5 \cdot 10^4$	Pa
left ventricle	n_f	contraction ratio along fibers	1	-
	n_n	contraction ratio along normals	0.4	-
	c	stiffness	$0.88 \cdot 10^3$	Pa
	p^0_LV	end-diastolic left ventricle pressure	8.63	mmHg
	$p^\mathrm{ref}_\mathrm{LV}$	reference left ventricle pressure	7.5	mmHg
left atrium	n_f	contraction ratio along fibers	1	-
	n_n	contraction ratio along normals	0.4	-
	c	Guccione stiffness	$1.76 \cdot 10^3$	Pa
	p^0_LA	end-diastolic left atrium pressure	9	mmHg
	$p^\mathrm{ref}_\mathrm{LA}$	reference left atrium pressure	6.75	mmHg
aorta	κ_NH	neo-Hooke bulk modulus	$10 \cdot 10^5$	Pa
	μ_NH	neo-Hooke stiffness	$5.25 \cdot 10^5$	Pa
	p^0_Ao	end-diastolic aortic pressure	71.26	mmHg
atrioventricular ring	κ_NH	neo-Hooke bulk modulus	$50 \cdot 10^5$	Pa
	μ_NH	neo-Hooke stiffness	$10 \cdot 10^5$	Pa
boundary conditions	K_epi	pericardium normal stiffness	$2 \cdot 10^5$	Pa/m
	C_epi	pericardium normal viscosity	$2 \cdot 10^3$	$\mathrm{Pa \cdot s/m}$
	$K^\mathrm{fat}_\mathrm{epi}$	epicardial fat normal stiffness	$2 \cdot 10^2$	Pa/m

Table A.6: Left heart test case. Parameters for the solid mechanics model.

[9] L. Bennati, C. Vergara, V. Giambruno, I. Fumagalli, A. F. Corno, A. Quarteroni, G. Puppini, and G. B. Luciani. An image-based computational fluid dynamics study of mitral regurgitation in presence of prolapse. *Cardiovascular Engineering and Technology*, 14(3):457–475, 2023.

[10] G. G. Blume, C. J. Mcleod, M. E. Barnes, J. B. Seward, P. A. Pellikka, P. M. Bastiansen, and T. S. Tsang. Left atrial function: physiology, assessment, and clinical implications. *European Journal of Echocardiography*, 12(6):421–430, 2011.

[11] M. Bucelli. The lifex library version 2.0. *arXiv preprint arXiv:2411.19624*, 2024.

[12] M. Bucelli, L. Dede', A. Quarteroni, and C. Vergara. Partitioned and monolithic FSI schemes for the numerical simulation of the heart. *Communications in Computational Physics*, 32(5):1217–1256, 2022.

[13] M. Bucelli, A. Zingaro, P. C. Africa, I. Fumagalli, L. Dede', and A. Quarteroni. A mathematical model that integrates cardiac electrophysiology, mechanics, and fluid dynamics: Application to the human left heart. *International Journal for Numerical Methods in Biomedical Engineering*, 39(3):e3678, 2023.

[14] A. Caballero, W. Mao, R. McKay, C. Primiano, S. Hashim, and W. Sun. New insights into mitral heart valve prolapse after chordae rupture through fluid–structure interaction computational modeling. *Scientific Reports*, 8(1):1–14, 2018.

Compartment	Parameter	Description	Value	Unit
right atrium	E_A	active elastance	0.06	mmHg/mL
	E_P	passive elastance	0.07	mmHg/mL
	t_C	relative duration of contraction	0.17	-
	t_R	relative duration of relaxation	0.17	-
	V_rest	resting volume	4	mL
	V_0	initial volume	64.1702	mL
right ventricle	E_A	active elastance	0.55	mmHg/mL
	E_P	passive elastance	0.05	mmHg/mL
	t_C	relative duration of contraction	0.34	-
	t_R	relative duration of relaxation	0.15	-
	V_rest	resting volume	16	mL
	V_0	initial volume	148.9384	mL
pulmonary arteries	R	resistance	0.05	$\mathrm{mmHg} \cdot \mathrm{s/mL}$
	C	capacitance	10.0	mL/mmHg
	R_up	upstream resistance	0.0	$\mathrm{mmHg} \cdot \mathrm{s/mL}$
	L	inductance	$5 \cdot 10^{-4}$	$\mathrm{mmHg} \cdot \mathrm{s/mL}^2$
	p_0	initial pressure	20	mmHg
	Q_0	initial flow rate	69.32	mmHg
pulmonary veins	R	resistance	0.025	$\mathrm{mmHg} \cdot \mathrm{s/mL}$
	C	capacitance	38.4	mL/mmHg
	L	inductance	$2.083 \cdot 10^{-4}$	$\mathrm{mmHg} \cdot \mathrm{s/mL}^2$
	p_0	initial pressure	17	mmHg
	Q_0	initial flow rate	105.52	mmHg
systemic arteries	R	resistance	0.45	$\mathrm{mmHg} \cdot \mathrm{s/mL}$
	C	capacitance	2.19	mL/mmHg
	R_up	upstream resistance	0.07	$\mathrm{mmHg} \cdot \mathrm{s/mL}$
	L	inductance	$2.7 \cdot 10^{-3}$	$\mathrm{mmHg} \cdot \mathrm{s/mL}^2$
	p_0	initial pressure	80	mmHg
	Q_0	initial flow rate	66.58	mmHg
systemic veins	R	resistance	0.26	$\mathrm{mmHg} \cdot \mathrm{s/mL}$
	C	capacitance	60.0	mL/mmHg
	L	inductance	$5 \cdot 10^{-4}$	$\mathrm{mmHg} \cdot \mathrm{s/mL}^2$
	p_0	initial pressure	30.90	mmHg
	Q_0	initial flow rate	89.63	mmHg

Table A.7: Left heart test case. Parameters for the circulation model. We refer to [25] for the meaning of each parameter.

[15] C. Chnafa, S. Mendez, and F. Nicoud. Image-based large-eddy simulation in a realistic left heart. *Computers & Fluids*, 94:173–187, 2014.

[16] M. Corti, L. Zingaro, Alberto Dede', and A. Quarteroni. Impact of atrial fibrillation on left atrium haemodynamics: A computational fluid dynamics study. *Computers in Biology and Medicine*, 150:106143, 2022.

[17] M. Courtemanche, R. J. Ramirez, and S. Nattel. Ionic mechanisms underlying human atrial action potential properties: insights from a mathematical model. *American Journal of Physiology-Heart and Circulatory Physiology*, 275(1):H301–H321, 1998.

[18] A. Crispino, L. Bennati, and C. Vergara. Cardiac hemodynamics computational modeling including chordae tendineae, papillaries, and valves dynamics. *bioRxiv*, pages 2024–05, 2024.

[19] L. Crugnola, C. Vergara, L. Fusini, I. Fumagalli, G. Luraghi, A. Redaelli, and G. Pontone. Computational hemodynamic indices to identify transcatheter aortic valve implantation degeneration. *Computer Methods and Programs in Biomedicine*, 259:108517, 2025.

[20] A. Daub, J. Kriegseis, and B. Frohnapfel. Replication of left ventricular haemodynamics with a simple planar mitral valve model. *Biomedical Engineering/Biomedizinische Technik*, 65(5):595–603, 2020.

[21] M. Davey, C. Puelz, S. Rossi, M. A. Smith, D. R. Wells, G. M. Sturgeon, W. P. Segars, J. P. Vavalle, C. S. Peskin, and B. E. Griffith. Simulating cardiac fluid dynamics in the human heart. *PNAS nexus*, 3(10):pgae392, 2024.

[22] J. Donea, S. Giuliani, and J.-P. Halleux. An arbitrary Lagrangian-Eulerian finite element method for transient dynamic fluid-structure interactions. *Computer Methods in Applied Mechanics and Engineering*, 33(1-3):689–723, 1982.

[23] F. Duca, D. Bissacco, L. Crugnola, C. Faitini, M. Domanin, F. Migliavacca, S. Trimarchi, and C. Vergara. Computational analysis to assess hemodynamic forces in descending thoracic aortic aneurysms. *The Journal of Physiology*, 2025.

[24] M. Fedele, E. Faggiano, L. Dede', and A. Quarteroni. A patient-specific aortic valve model based on moving resistive immersed implicit surfaces. *Biomechanics and Modeling in Mechanobiology*, 16(5):1779–1803, 2017.

[25] M. Fedele, R. Piersanti, F. Regazzoni, M. Salvador, P. C. Africa, M. Bucelli, A. Zingaro, L. Dede', and A. Quarteroni. A comprehensive and biophysically detailed computational model of the whole human heart electromechanics. *Computer Methods in Applied Mechanics and Engineering*, 410:115983, 2023.

[26] M. Fedele and A. Quarteroni. Polygonal surface processing and mesh generation tools for the numerical simulation of the cardiac function. *International Journal for Numerical Methods in Biomedical Engineering*, 37(4):e3435, 2021.

[27] L. Feng, H. Gao, and X. Luo. Whole-heart modelling with valves in a fluid–structure interaction framework. *Computer Methods in Applied Mechanics and Engineering*, 420:116724, 2024.

[28] D. Forti and L. Dede'. Semi-implicit bdf time discretization of the navier–stokes equations with vms-les modeling in a high performance computing framework. *Computers & Fluids*, 117:168–182, 2015.

[29] I. Fumagalli, L. Dede', and A. Quarteroni. A reduced 3D-0D fluid–structure interaction model of the aortic valve that includes leaflet curvature. *Biomechanics and Modeling in Mechanobiology*, 2025.

[30] I. Fumagalli, M. Fedele, C. Vergara, L. Dede', S. Ippolito, F. Nicolò, C. Antona, R. Scrofani, and A. Quarteroni. An image-based computational hemodynamics study of the systolic anterior motion of the mitral valve. *Computers in Biology and Medicine*, 123:103922, 2020.

[31] T. Gerach, S. Schuler, J. Fröhlich, L. Lindner, E. Kovacheva, R. Moss, E. M. Wülfers, G. Seemann, C. Wieners, and A. Loewe. Electro-mechanical whole-heart digital twins: a fully coupled multi-physics approach. *Mathematics*, 9(11):1247, 2021.

[32] C. Geuzaine, J.-F. Remacle, and P. Dular. Gmsh: a three-dimensional finite element mesh generator. *International Journal for Numerical Methods in Engineering*, 79(11):1309–1331, 2009.

[33] T. J. R. Hughes, W. K. Liu, and T. K. Zimmermann. Lagrangian-Eulerian finite element formulation for incompressible viscous flows. *Computer Methods in Applied Mechanics and Engineering*, 29(3):329–349, 1981.

[34] R. Izzo, D. Steinman, S. Manini, and L. Antiga. The vascular modeling toolkit: a Python library for the analysis of tubular structures in medical images. *Journal of Open Source Software*, 3(25):745, 2018.

[35] E. L. Johnson, D. W. Laurence, F. Xu, C. E. Crisp, A. Mir, H. M. Burkhart, C.-H. Lee, and M.-C. Hsu. Parameterization, geometric modeling, and isogeometric analysis of tricuspid valves. *Computer methods in applied mechanics and engineering*, 384:113960, 2021.

[36] E. Karabelas, S. Longobardi, J. Fuchsberger, O. Razeghi, C. Rodero, M. Strocchi, R. Rajani, G. Haase, G. Plank, and S. Niederer. Global sensitivity analysis of four chamber heart hemodynamics using surrogate models. *IEEE Transactions on Biomedical Engineering*, 2022.

[37] J. Kronborg and J. Hoffman. Fluid-structure interaction simulation of mitral valve structures in a left ventricle model. *International Journal for Numerical Methods in Engineering*, 126(8):e70031, Apr. 2025.

[38] V. Meschini, M. De Tullio, G. Querzoli, and R. Verzicco. Flow structure in healthy and pathological left ventricles with natural and prosthetic mitral valves. *Journal of Fluid Mechanics*, 834:271–307, 2018.

[39] D. Oks, C. Samaniego, G. Houzeaux, C. Butakoff, and M. Vázquez. Fluid–structure interaction analysis of eccentricity and leaflet rigidity on thrombosis biomarkers in bioprosthetic aortic valve replacements. *International Journal for Numerical Methods in Biomedical Engineering*, 38(12):e3649, 2022.

[40] P. S. Pagel, F. Kehl, M. Gare, D. A. Hettrick, J. R. Kersten, and D. C. Warltier. Mechanical function of the left atrium: new insights based on analysis of pressure-volume relations and doppler echocardiography. *Anesthesiology*, 98(4):975–994, 2003.

[41] G. Pase, E. Brinkhuis, T. De Vries, J. Kosinka, T. Willems, and C. Bertoglio. A parametric geometry model of the aortic valve for subject-specific blood flow simulations using a resistive approach. *Biomechanics and Modeling in Mechanobiology*, 22(3):987–1002, 2023.

[42] R. Piersanti, P. C. Africa, M. Fedele, C. Vergara, L. Dede', A. F. Corno, and A. Quarteroni. Modeling cardiac muscle fibers in ventricular and atrial electrophysiology simulations. *Computer Methods in Applied Mechanics and Engineering*, 373:113468, 2021.

[43] R. Piersanti, F. Regazzoni, M. Salvador, A. F. Corno, C. Vergara, and A. Quarteroni. 3D–0D closed-loop model for the simulation of cardiac biventricular electromechanics. *Computer Methods in Applied Mechanics and Engineering*, 391:114607, 2022.

[44] F. Regazzoni, L. Dede', and A. Quarteroni. Biophysically detailed mathematical models of multiscale cardiac active mechanics. *PLoS Computational Biology*, 16(10):e1008294, 2020.

[45] F. Regazzoni, M. Salvador, P. C. Africa, M. Fedele, L. Dede', and A. Quarteroni. A cardiac electromechanical model coupled with a lumped-parameter model for closed-loop blood circulation. *Journal of Computational Physics*, 457:111083, 2022.

[46] F. Renzi, C. Vergara, M. Fedele, V. Giambruno, A. Quarteroni, G. Puppini, and G. B. Luciani. Accurate reconstruction of right heart shape and motion from Cine-MRI for image-driven computational hemodynamics. *International Journal for Numerical Methods in Biomedical Engineering*, 41(1):e3891, 2025.

[47] O. Ruz, J. Diaz, M. Vidrascu, P. Moireau, D. Chapelle, and M. A. Fernández. Left heart hemodynamics simulations with fluid-structure interaction and reduced valve modeling. *HAL preprint hal-04733426*, 2024.

[48] M. Salvador, F. Regazzoni, S. Pagani, L. Dede', N. Trayanova, and A. Quarteroni. The role of mechano-electric feedbacks and hemodynamic coupling in scar-related ventricular tachycardia. *Computers in Biology and Medicine*, 142:105203, 2022.

[49] J. H. Seo, V. Vedula, T. Abraham, A. C. Lardo, F. Dawoud, H. Luo, and R. Mittal. Effect of the mitral valve on diastolic flow patterns. *Physics of Fluids*, 26(12), 2014.

[50] J. H. Spühler, J. Jansson, N. Jansson, and J. Hoffman. 3D fluid-structure interaction simulation of aortic valves using a unified continuum ALE FEM model. *Frontiers in Physiology*, 9:363, 2018.

[51] K. Stein, T. Tezduyar, and R. Benney. Mesh moving techniques for fluid-structure interactions with large displacements. *Journal of Applied Mechanics*, 70(1):58–63, 2003.

[52] S. Stella, F. Regazzoni, C. Vergara, L. Dede', and A. Quarteroni. A fast cardiac electromechanics model coupling the eikonal and the nonlinear mechanics equations. *Mathematical Models and Methods in Applied Sciences*, 32(08):1531–1556, 2022.

[53] M. Strocchi, M. A. Gsell, C. M. Augustin, O. Razeghi, C. H. Roney, A. J. Prassl, E. J. Vigmond, J. M. Behar, J. S. Gould, C. A. Rinaldi, et al. Simulating ventricular systolic motion in a four-chamber heart model with spatially varying robin boundary conditions to model the effect of the pericardium. *Journal of Biomechanics*, 101:109645, 2020.

[54] M. Strocchi, S. Longobardi, C. M. Augustin, M. A. Gsell, A. Petras, C. A. Rinaldi, E. J. Vigmond, G. Plank, C. J. Oates, R. D. Wilkinson, et al. Cell to whole organ global sensitivity analysis on a four-chamber heart electromechanics model using gaussian processes emulators. *PLoS Computational Biology*, 19(6):e1011257, 2023.

[55] K. H. Ten Tusscher and A. V. Panfilov. Alternans and spiral breakup in a human ventricular tissue model. *American Journal of Physiology-Heart and Circulatory Physiology*, 291(3):H1088–H1100, 2006.

[56] T. Terahara, T. Kuraishi, K. Takizawa, and T. E. Tezduyar. Computational flow analysis with boundary layer and contact representation: II. heart valve flow with leaflet contact. *Journal of Mechanics*, 38:185–194, 2022.

[57] A. This, L. Boilevin-Kayl, M. A. Fernández, and J.-F. Gerbeau. Augmented resistive immersed surfaces valve model for the simulation of cardiac hemodynamics with isovolumetric phases. *International Journal for Numerical Methods in Biomedical Engineering*, 36(3):e3223, 2020.

[58] M. Toma, D. R. Einstein, C. H. Bloodworth IV, R. P. Cochran, A. P. Yoganathan, and K. S. Kunzelman. Fluid–structure interaction and structural analyses using a comprehensive mitral valve model with 3D chordal structure. *International Journal for Numerical Methods in Biomedical Engineering*, 33(4):e2815, 2017.

[59] T. P. Usyk, I. J. LeGrice, and A. D. McCulloch. Computational model of three-dimensional cardiac electromechanics. *Computing and Visualization in Science*, 4(4):249–257, 2002.

[60] V. Vedula, J.-H. Seo, A. C. Lardo, and R. Mittal. Effect of trabeculae and papillary muscles on the hemodynamics of the left ventricle. *Theoretical and Computational Fluid Dynamics*, 30(1):3–21, 2016.

[61] K. Vellguth, J. Brüning, L. Goubergrits, L. Tautz, A. Hennemuth, U. Kertzscher, F. Degener, M. Kelm, S. Sündermann, and T. Kuehne. Development of a modeling pipeline for the prediction of hemodynamic outcome after virtual mitral valve repair using image-based CFD. *International Journal of Computer Assisted Radiology and Surgery*, 13:1795–1805, 2018.

[62] A. Zingaro, Z. Ahmad, E. Kholmovski, K. Sakata, L. Dede', A. K. Morris, A. Quarteroni, and N. A. Trayanova. A comprehensive stroke risk assessment by combining atrial computational fluid dynamics simulations and functional patient data. *Scientific Reports*, 14(1):9515, 2024.

[63] A. Zingaro, M. Bucelli, R. Piersanti, F. Regazzoni, L. Dede', and A. Quarteroni. An electromechanics-driven fluid dynamics model for the simulation of the whole human heart. *Journal of Computational Physics*, 454:112885, 2024.

[64] A. Zingaro, I. Burba, D. Oks, M. Fontana, C. Samaniego, M. Bischofberger, B. de Boeck, A. Douverny, Ö. Karakas, S. Toggweiler, D. Arzamendi-Aizpurua, U. Gülan, and M. Vázquez. Advancing aortic stenosis assessment: validation of fluid-structure interaction models against 4D flow MRI data. *arXiv preprint arXiv:2404.08632*, 2024.

[65] A. Zingaro, I. Fumagalli, L. Dede', M. Fedele, P. C. Africa, A. F. Corno, and A. Quarteroni. A geometric multiscale model for the numerical simulation of blood flow in the human left heart. *Discrete and Continuous Dynamical Systems*, 15(8):2391–2427, 2022.

[66] Zygote Media Group Inc. Zygote solid 3D heart generation II developement report. Technical report. 2014.

MOX Technical Reports, last issues

Dipartimento di Matematica
Politecnico di Milano, Via Bonardi 9 - 20133 Milano (Italy)

33/2025 Di Battista, I.; De Sanctis, M.F.; Arnone, E.; Castiglione, C.; Palummo, A.; Sangalli, L.M.
A semiparametric space-time quantile regression model

32/2025 De Sanctis, M.F.; Di Battista, I.; Arnone, E.; Castiglione, C.; Palummo, A.; Bernardi, M.; Ieva, F.; Sangalli, L.M.
Exploring nitrogen dioxide spatial concentration via physics-informed multiple quantile regression

31/2025 Botteghi, N.; Fresca, S.; Guo, M.; Manzoni, A.
HypeRL: Parameter-Informed Reinforcement Learning for Parametric PDEs

30/2025 Rosafalco, L.; Conti, P.; Manzoni, A.; Mariani, S.; Frangi, A.
Online learning in bifurcating dynamic systems via SINDy and Kalman filtering

29/2025 Centofanti, E.; Ziarelli, G.; Parolini, N.; Scacchi, S.; Verani, M. ; Pavarino, L. F.
Learning cardiac activation and repolarization times with operator learning

28/2025 Ciaramella, G.; Gander, M.J.; Mazzieri, I.
Discontinuous Galerkin time integration for second-order differential problems: formulations, analysis, and analogies

27/2025 Antonietti P.F.; Artoni, A.; Ciaramella, G.; Mazzieri, I.
A review of discontinuous Galerkin time-stepping methods for wave propagation problems

24/2025 Bartsch, J.; Borzi, A.; Ciaramella, G.; Reichle, J.
Adjoint-based optimal control of jump-diffusion processes

22/2025 Leimer Saglio, C. B.; Pagani, S.; Antonietti P. F.
A p-adaptive polytopal discontinuous Galerkin method for high-order approximation of brain electrophysiology

23/2025 Antonietti, P. F.; Caldana, M.; Mazzieri, I.; Re Fraschini, A.
MAGNET: an open-source library for mesh agglomeration by Graph Neural Networks